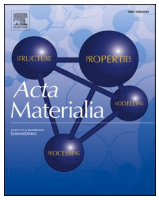
Acta Materialia 285 (2025) 120662



Contents lists available at ScienceDirect

Acta Materialia

journal homepage: www.elsevier.com/locate/actamat



Passivating oxidation behavior of $Ti_{0.12}Al_{0.21}B_{0.67}$ coatings investigated by scanning transmission electron microscopy and chemical environment dependent density functional theory simulations

Sebastian Lellig [a,b], Amir Hossein Navidi Kashani [a], Peter Schweizer [b], Marcus Hans [a], Ganesh K. Nayak [a], Johann Michler [b,c], Jochen M. Schneider [a,d]

[a] Materials Chemistry, RWTH Aachen University, Germany
[b] Empa, Swiss Federal Laboratories for Materials Science and Technology, Laboratory for Mechanics of Materials and Nanostructures, Feuerwerkerstrasse 39, Thun 3602, Switzerland
[c] École Polytechnique Fédérale de Lausanne (EPFL), Lausanne 1015, Switzerland
[d] Department Structure and Nano-/ Micromechanics of Materials, Group Self-Reporting Materials, Max-Planck-Institute for sustainable materials GmbH, Düsseldorf, Germany

ARTICLE INFO

Keywords:
Oxidation
Scanning transition electron microscope
Atom probe tomography
B-containing oxide scale
Protective coatings
Transition metal diborides

ABSTRACT

The oxidation behavior of stoichiometric $Ti_{0.12}Al_{0.21}B_{0.67}$ coatings is investigated by scanning transmission electron microscopy (STEM) after oxidizing for 1, 4 and 8 h at 700 °C and at 800 and 900 °C.

In the as deposited state, a ~4 nm thick, native, amorphous oxide layer covers the surface of the coating, while the magnitude of incorporated O along the column boundaries decreases with depth. During oxidation, the formation of scale layers consisting predominantly of Al, O and B is observed, that appear to be amorphous at 700 °C, while after oxidation at 900 °C for 8 h, a (nano-)crystalline aluminoborate layer forms. Concurrently, within the unoxidized coating, the formation of Al- and Ti-rich boride regions, consistent with spinodal decomposition, is observed. Chemical environment dependent density functional theory (DFT) predictions of the energies required for mass transport on the metal sublattice indicate that Al diffusion is initiated before Ti diffusion. Hence, as the temperature is increased, the migration of Al is initiated first, leading to the formation of the oxide scale observed already after oxidation at 700 °C for 1 h. Below the oxidized region, the formation of Al-rich and Ti-rich regions by spinodal decomposition require the concurrent migration of Al and Ti. The fact that decomposition takes place at 900 °C and hence at larger temperatures than the Al diffusion mediated scale formation is consistent with DFT predictions as the average values of the predicted energies required for both, vacancy formation and migration for Ti, are larger than for Al.

1. Introduction

Due to their outstanding thermal stability, transition metal diborides (TMB_2) are employed in (ultra) high-temperature applications [1–3]. For example, titanium diboride (TiB_2) has been extensively studied as a protective coating material for cutting tools [4–6], whereby temperatures may exceed 1000 °C at the cutting edge [7], protective shields for space applications [8] or as a functionally graded armor ceramic [9] due to its melting point of > 3000 °C [10], exceptional thermal stability [11,12] and outstanding mechanical properties [11–14]. The application of TiB_2 as a cathode material for aluminum electrolysis with temperatures up to 1400 °C [15–18] and its potential use as a protective coating for metallic bipolar plates in proton-exchange membrane fuel cells (PEMFCs) [19] is enabled by the considerable chemical stability and corrosion resistance [3,19–21]. However, during exposure to atmosphere at elevated temperatures, the oxidation behavior of bulk TiB_2 was reported by Cai et al. [22] to be highly dependent on the configuration of the scale. Compared to 650 °C, the oxidation rate at 500 °C increased considerably, which was attributed to be due to the formation of a Ti-B-O amorphous inner layer and a dual-phase top layer containing amorphous B_2O_3 and rutile TiO_2. At 800 °C, a scale thickness of approximately 10 μm is measured after 1 hour of oxidation [22].

Hexagonal TiB_2 (space group P6/mmm) thin films were produced by magnetron sputtering, possessing a columnar nanostructure [11]. The formation of an amorphous, boron-rich tissue phase, located between column boundaries, was observed for thin films with an excess of boron [11]. It was reported that the tissue phase leads to a significant increase in hardness from 43.4 ± 0.8 GPa ($TiB_{1.97}$) [14] to > 60 GPa ($TiB_{2.4-3.2}$) [11]. Furthermore, Fuger et al. reported a significant hardness-anisotropy for TiB_z films with z varying from 2.07 to 4.42

https://doi.org/10.1016/j.actamat.2024.120662
Received 17 September 2024; Received in revised form 10 December 2024; Accepted 16 December 2024
Available online 18 December 2024
1359-6454/© 2024 The Authors. Published by Elsevier Ltd on behalf of Acta Materialia Inc. This is an open access article under the CC BY license (http://creativecommons.org/licenses/by/4.0/).

based on an increase in film hardness of > 10 GPa with increasing {0001} fraction [23].

Upon oxidation, the scale formed is mostly composed of B_2O_3 and TiO_2, whereby oxidation is initiated at 400 °C [24]. At 500 °C, Bakhit et al. reported that $TiB_{2.4}$ films, containing a B-rich tissue phase, formed B-deficient and porous scales, which was attributed to evaporation of volatile B_2O_3 [25]. Similarly, Voitovich et al. observed a decrease in the amount of B_2O_3 in comparison to TiO_2 in the scale after oxidation in the temperature range of 950 to 1100 °C [26].

It has been shown, that the addition of Al to TiB_2 thin films leads to a significant reduction of the oxide scale thickness [24,25,27–29] and a concurrent decrease in both, hardness and Young's modulus in comparison to TiB_2 [25,30,31].

With regard to thermal stability of a $(Ti_{0.71}Al_{0.29})B_{3.08}$ coating, Mockuté et al. observed phase separation after annealing at 1000 °C for 1 h. The formation of Ti-deficient crystallites observed within (Ti,Al)B_2 columns, which are in turn embedded in the B-rich tissue phase, was ascribed to be due to nucleation and growth via grain boundary diffusion and surface-directed decomposition [32].

Bakhit et al. [25] compared the oxide scale thickness formed on over-stoichiometric $TiB_{2.4}$, containing a B-rich tissue phase, with B-deficient $Ti_{0.68}Al_{0.32}B_{1.35}$ after oxidizing at 700 °C for 1 h. The authors attributed the improved oxidation behavior to be due to the formation of an X-ray amorphous, dense oxide layer containing Al, hindering coarsening of the oxide, below a more porous outer layer. Additionally, it was reported that the film containing Al possessed Ti-rich grain boundaries encapsulated in an Al-rich and B-deficient tissue phase in contrast to the B-rich $TiB_{2.4}$ film exhibiting a B-rich tissue phase [25]. Hence, it is reasonable to assume that the improved oxidation behavior in $Ti_{0.9}Al_{0.1}B_{1.3}$ compared to $TiB_{2.4}$ is due to the combined effect of Al incorporation and the lack of a B-rich tissue phase.

The influence of the B concentration on the oxide scale formation during oxidation at 600 °C for 10 h was studied by Thörnberg et al. [28]. They investigated $Ti_{0.9}Al_{0.1}B_{1.9}$, exhibiting a B-rich tissue phase, despite the under-stoichiometric composition, and $Ti_{0.9}Al_{0.1}B_{1.3}$, without a tissue phase, and observed oxide scales composed of a TiO_2 and Al_2O_3-TiO_2 double layer with thicknesses of ~320 nm and ~ 140 nm, respectively. Additionally, B_2O_3 was suggested to be present at the interface between the two oxide layers [28]. The improvement in the oxidation resistance of $Ti_{0.9}Al_{0.1}B_{1.3}$ compared to $Ti_{0.9}Al_{0.1}B_{1.9}$ was attributed to the absence of the boron-rich tissue phase in the more B-deficient film [28].

Navidi et al. [27] systematically investigated the influence of deviations from stoichiometry on oxidation behavior and mechanical properties of $(Ti_{0.35}Al_{0.65})B_y$ thin films considering besides $y = 2.0$ over- ($y = 2.4$) and under-stoichiometric ($y = 1.7$) compositions. $(Ti_{0.35}Al_{0.65})B_{2.0}$ possessed an elastic modulus of 395 ± 12 GPa, which was higher than the moduli of the B-rich $(Ti_{0.34}Al_{0.66})B_{2.4}$ and the B-deficient $(Ti_{0.36}Al_{0.64})B_{1.7}$ with 330 ± 9 GPa and 274 ± 16 GPa, respectively. This trend is in good agreement with ab initio calculations resulting in theoretical values for the elastic modulus of 253 GPa for the B-deficient $(Ti_{0.36}Al_{0.64})B_{1.7}$ and 353 GPa for the stoichiometric $(Ti_{0.35}Al_{0.65})B_{2.0}$ coating. The lower elastic modulus for the B-deficient compositions can be rationalized by bond weakening as witnessed by composition induced changes in cohesive energy. The elastic modulus reduction for the B-rich coating reported in [27] was, consistent with Nedfors et al. [31], ascribed to the presence of B-rich tissue phase.

The stoichiometric $(Ti_{0.35}Al_{0.65})B_{2.0}$ thin film reported [27], showed an oxide scale consisting mostly of Al and O and a thickness of 39 ± 7 nm, which was similar to the B-deficient sample (40 ± 4 nm) in comparison to 204 ± 16 nm for the B-rich $(Ti_{0.34}Al_{0.66})B_{2.4}$ coating after oxidizing at 700 °C for 8 h, clearly outperforming titanium aluminum nitride coatings with a similar Al/Ti ratio. The considerable reduction in oxidation resistance observed for the B-rich coating was attributed, in line with Bakhit et al. [25], to be due to the presence of boron-rich tissue phases. Overall, the stoichiometric $(Ti_{0.35}Al_{0.65})B_{2.0}$ coating composition proved superior in comparison to both, the B-rich and the B-deficient coatings, when oxidation resistance and mechanical behavior are considered jointly [27]. Navidi et al. [33] revealed the influence of the Al content in stoichiometric $Ti_{0.33-x}Al_xB_{0.67}$ coatings with x = 0.04, 0.15, 0.21, and 0.28 upon oxidation at temperatures up to 900 °C for 8 h. For $x \geq 21$ at.%, the formation of a passivating, X-ray amorphous oxide scale was observed, while for $x \leq 15$ at.% a non-passivating, crystalline oxide scale was formed. This scale showed besides the presence of pores also Al-rich and Ti-rich oxide regions [33].

While oxidation resistance data for TiB_2 with additions of Al have been reported for temperatures up to 900 °C [22,24,30], and the passivation requirements in terms of the Al concentration have been communicated for this temperature range [30], little is known regarding the underlying, atomic scale mechanisms enabling passivating oxidation behavior of stoichiometric (Ti,Al)B_2 coatings.

Here, high-resolution studies have been performed before and after oxidation of $Ti_{0.12}Al_{0.21}B_{0.67}$ coatings. Specifically, transmission electron microscopy (TEM) analyses including energy X-ray dispersive spectroscopy (EDX) mappings and scanning transmission electron microscopy (STEM) as well as atom probe tomography (APT) were utilized to analyze changes in local chemical composition occurring during scale formation upon oxidation at 700, 800 and 900 °C for up to 8 h. The temporal evolution of spatially resolved composition and structure data were compared to density functional theory (DFT) statistical envelope calculations [34,35] of the formation energy of vacancies as well as the activation energy of migration to identify the atomistic mechanisms enabling scale formation.

2. Experimental details

The protocol employed for the synthesis of the boride coatings using magnetron sputtering of two B targets and a $Ti_{0.4}Al_{0.6}$ target in an ultra-high vacuum growth system was described by Navidi et al. [27]. With target power densities of 8.5 W/cm^2 for the B targets and 2 W/cm^2 for the $Ti_{0.4}Al_{0.6}$ target, a composition of 11.6 ± 1.2 at.% Ti, 21.4 ± 2.2 at.% Al and 67.0 ± 3.4 at.% B, based on elastic recoil detection analysis (ERDA), was obtained and is henceforth referred to as stoichiometric $Ti_{0.12}Al_{0.21}B_{0.67}$ [27].

Different $Ti_{0.12}Al_{0.21}B_{0.67}$ coatings were oxidized in ambient air at 700 °C for 1, 4 and 8 h as well as for 8 h at 800 and 900 °C in a GERO (SR70–200/12) tube furnace. To this end, an Al_2O_3 crucible containing one sample was introduced together with a Ni/Ni-Cr thermocouple located on the same height as the crucible into the pre-heated furnace and removed after the corresponding oxidation time.

For the structural and chemical analysis of the coatings, STEM imaging, selected area electron diffraction (SAED) as well as EDX mapping were performed using a Thermo Fisher Scientific Titan Themis 200 G3 equipped with a SuperX detector. Therefore, lamellae were prepared by focused ion beam (FIB) milling using a FEI Helios Nanolab 660 dual-beam microscope as well as a Tescan Lyra FIB/scanning electron microscope (SEM), whereby Pt was deposited as a protective layer. The lamellae were thinned to around 50 nm and polished with a voltage of 5 kV. The oxide scale thickness values are based on ten individual measurements and the scale thickness range given corresponds to one standard deviation. For the chemical composition ranges determined by EDX within a region of interest, average values are given as well as the minimum and maximum values for each line scan.

Three-dimensional chemical composition analysis at the nanometer scale was carried out by APT and specimens were prepared in plan-view lift-out geometry (see supplementary information of [34]) at a distance of ~300 nm from the surface/interface of the unoxidized coating region. This lift-out geometry was chosen in order to maximize the number of grain boundaries as the coatings exhibit columnar grains. Atom probe specimens were prepared by FIB techniques using the FEI Helios Nanolab 660 dual-beam microscope according to a standard protocol [36]. Low voltage cleaning at 5 kV and 40 pA has been carried out for 10 min in order to achieve needle-like specimens with radius and shank

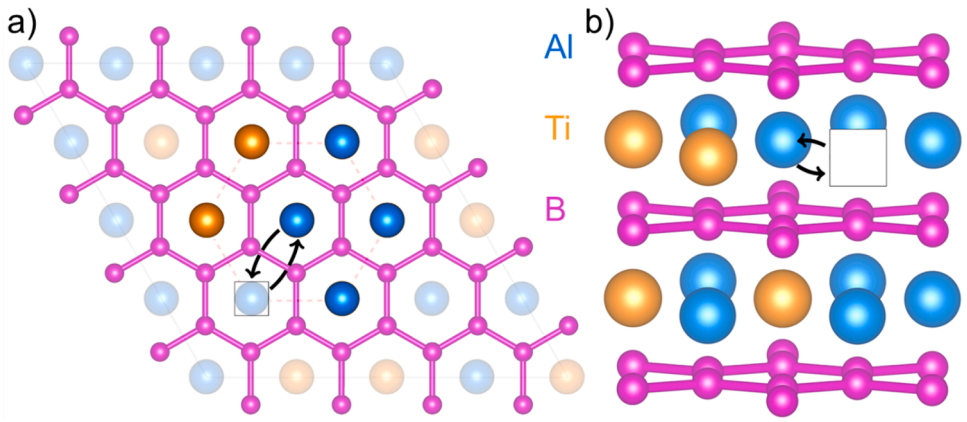


Fig. 1. Schematic representation of the chemical environment around the diffusing Al atom (in the middle) to its adjacent lattice side from the top view (a) and side view (b).

angle of < 30 nm and $< 10°$, respectively. Field evaporation was done using a CAMECA local electrode atom probe (LEAP)4000X HR and assisted by thermal pulsing with a UV laser at 50 pJ pulse energy, 125 kHz laser pulse frequency, 60 K base temperature and the detection rate was set at 0.5 %. While 10 million ions could be acquired for the coating oxidized at 700 °C for 8 h, only 1 million ions were collected for the as deposited coating and for the coating oxidized at 900 °C for 8 h due to premature fracture of the specimens. Reconstructions and data analysis were done with AP Suite 6.1.

3. Computational details

The vacancy formation energy (E_f) and activation energy of migration (E_b) calculation presented in this work is based on statistical envelope calculations, which were introduced in references [34,35]). To this end, Ti in hexagonal TiB_2 (space group P6/mmm) is partly substituted by Al. The random $(Ti,Al)B_2$ solid solution configuration was obtained with the special quasi-random structure (SQS) method [37]. To mimic the desired experimental composition, i.e., $Ti_{0.12}Al_{0.21}B_{0.67}$, the metal sublattice is populated with 17 Al atoms and 10 Ti atoms in a single-crystal model of $(Ti,Al)B_2$ with a supercell of $3 \times 3 \times 3$.

To calculate E_f and E_b, DFT was used as implemented in the Vienna ab initio simulation package (VASP) [38,39]. Generalized gradient approximation (GGA)-Perdew-Burke-Ernzerhof (PBE) [40] parameterization has been used to describe the electron-electron exchange and correlation interactions. The pseudo-potentials used for each of the elements in the calculations treat any semi-core states as valence, and the recommended potential is used as per the VASP website recommendation. The ion-electron interactions were described using the projector augmented wave method [41], with a plane-wave energy cut-off of 500 eV. The corresponding Brillouin zone was with $7 \times 7 \times 7$ Monkhorst–Pack k-point mesh [42]. The Methfessel–Paxton [43] smearing of 0.2 eV was applied. A convergence criterion of 10^{-6} eV (per supercell) was used for the total energy during the electronic self-consistency cycles and ionic relaxations during structural optimizations, and the total energy convergence of 10^{-4} eV (per supercell) was applied. All calculations were non-magnetic.

First, a vacancy was created at each of the 81 sites (27 metal, 54 non-metal) and E_f is calculated separately as $E_f = E_i - E_0 + \mu_i$, where E_i and E_0 are the total energy of the supercell with and without the vacancy, respectively, and μ_i is the chemical potential of the species i. The chemical potential for each species was conventionally set equal to the energy-per-atom of the corresponding element in its stable solid structure. E_b was calculated using the nudged elastic band (NEB) method [44]. The envelope approach [34,35] is designed so that the migrating atom diffuses to another vacant site only if that site was occupied by the same species in the parent (vacancy-free) supercell, see Fig. 1. Here, it can be seen that depending on the trajectory, the chemical environment differs, which in turn affects the magnitude of E_b. Also, the energy required to form a vacancy is chemical environment dependent. The variability induced by changes in chemical environment for both energies are collected in the envelope for each element. The cells were relaxed regarding size, shape, and atomic positions before vacancy and migration barrier calculations.

The transition state corresponding to the saddle point along the minimum energy diffusion path was determined using the NEB [44]

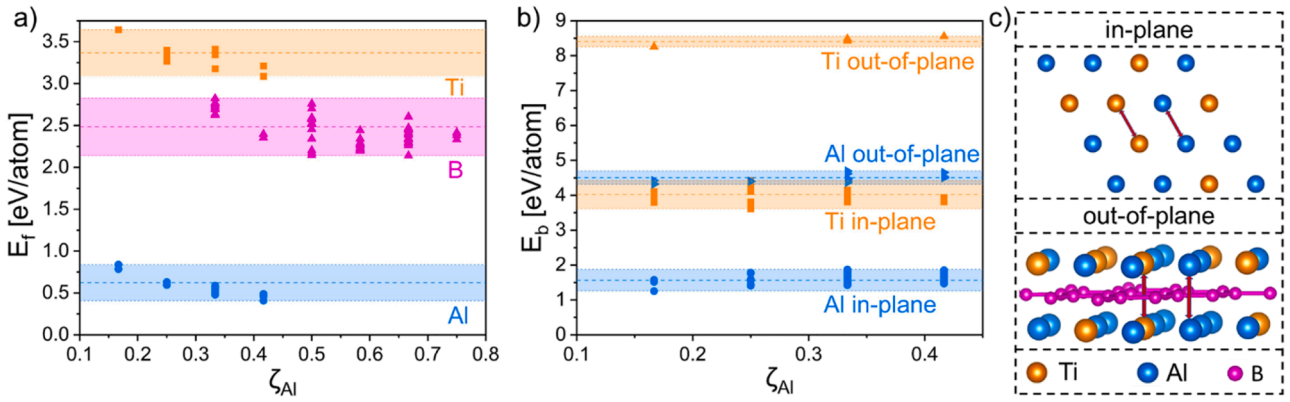


Fig. 2. Formation energy of vacancies for Ti, B and Al in $Ti_{0.12}Al_{0.21}B_{0.67}$ (a) as well as activation energy of migration of Al and Ti atoms (b) in dependence of the Al-fraction of the local chemical environment ζ_{Al}. For the activation energy, in-plane (within the metal lattice) and out-of-plane movement (through the B lattice) has to be differentiated (c).

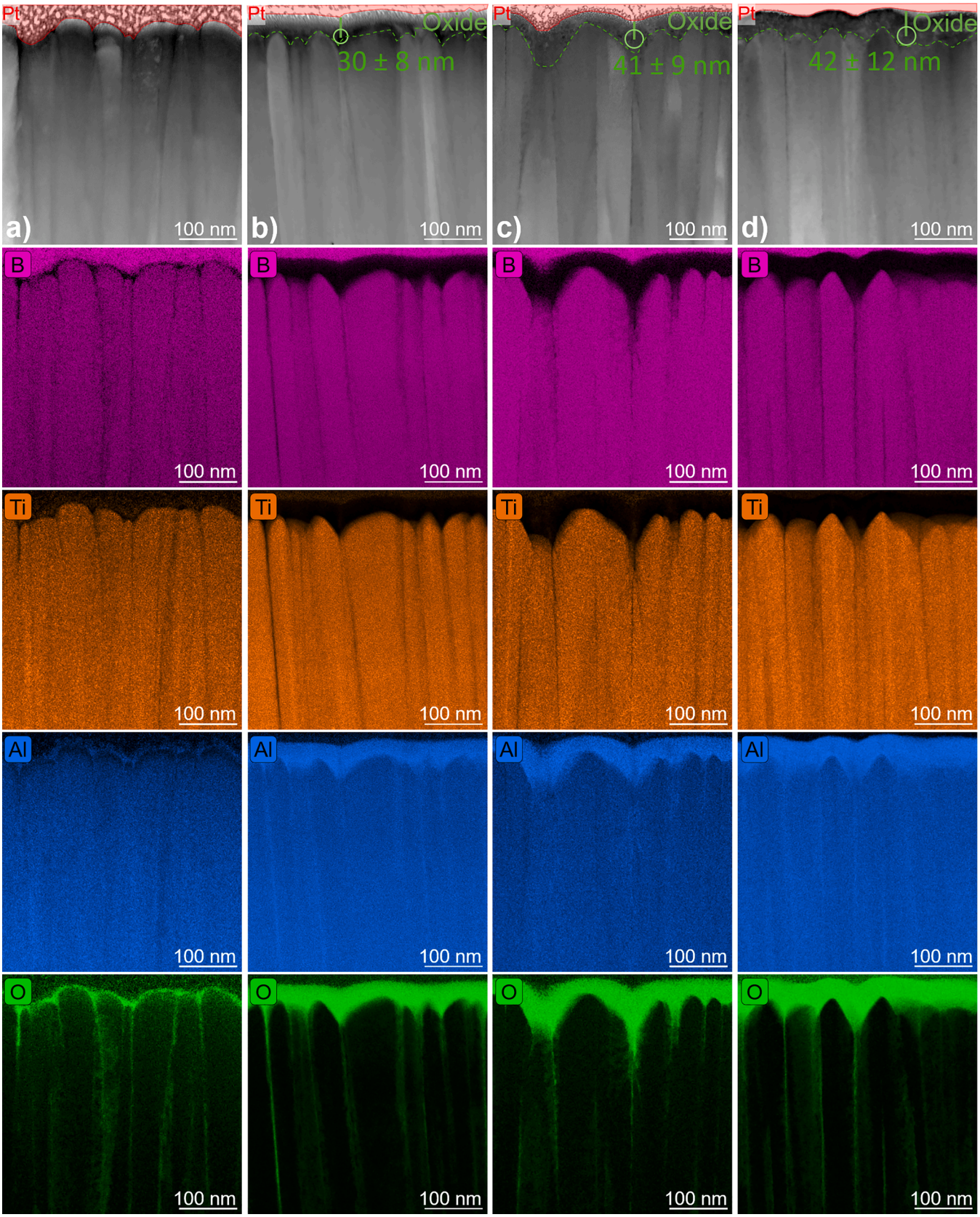


Fig. 3. HAADF images and EDX maps in at.% of a) as deposited sample and oxidized samples at 700 °C for b) 1 h c) 4 h and d) 8 h. The protective Pt layer is colored in red.

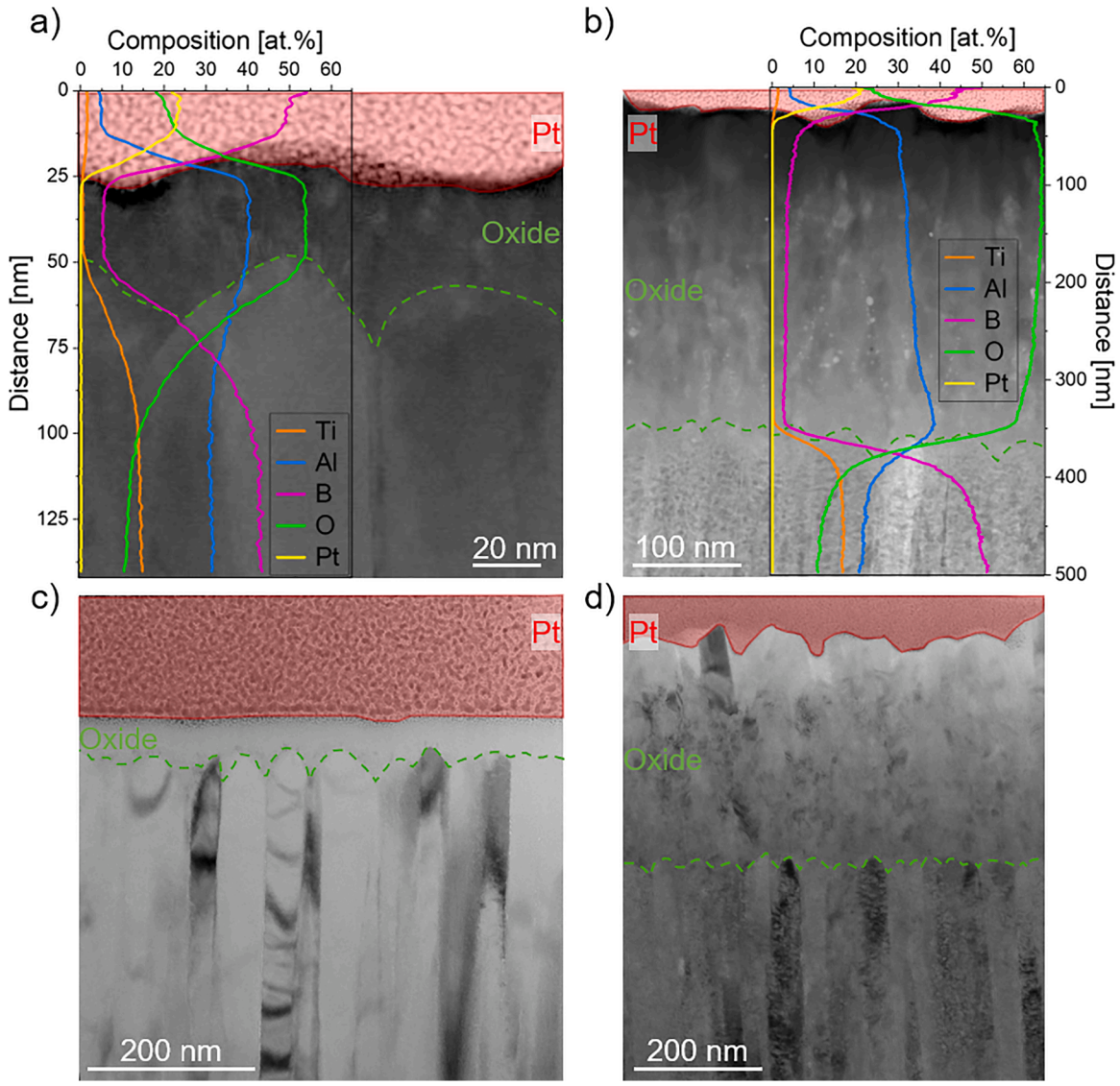


Fig. 4. a) EDX line scan of oxidized sample (700 °C, 8 h): Oxide layer consists primarily of Al and O. b) Composition of the oxide layer after oxidation at 900 °C for 8 h. c) and d) TEM images of the oxide layer morphology: after annealing at 700 °C for 8 h, the oxide layer is smooth (c), while after oxidation at 900 °C for 8 h, faceting is observed (d).

method implemented in VASP, following the protocol laid out in [45].

4. Results and discussion

To investigate the mechanisms active during oxidation of stoichiometric $Ti_{0.12}Al_{0.21}B_{0.67}$, DFT envelope calculations were conducted. Here, the envelope captures the impact of different chemical environments encountered in the ternary solid solution during vacancy formation and migration. As is shown in Fig. 2(a), the formation energy envelope for vacancies is significantly lower for Al as compared to B and Ti. For the formation of Al vacancies, the minimum and maximum energies required are 0.41 and 0.84 eV/atom, respectively, corresponding to an 0.62 ± 0.22 eV/atom envelope. The corresponding envelopes for Ti and B are 3.37 ± 0.28 and 2.48 ± 0.34 eV/atom, respectively. Hence, on the metal sublattice the formation of Al vacancies is predicted to take place at lower temperatures than the formation of Ti vacancies. Similarly to the vacancy formation predictions, the activation energy of migration is predicted to be lower for Al compared to Ti, see Fig. 2(b). Hereby, the in-plane and out-of-plane movement needs to be differentiated, see Fig. 2(c). In-plane movement describes the transfer from a metal atom to a free vacancy of the same type in the metal lattice. For out-of-plane movement, metal atoms must transit through a B layer, see Fig. 2(c). The energy for migration for out-of-plane movement is significantly higher for Ti with 8.41 ± 0.15 eV/atom than for Al with 4.51 ± 0.19 eV/atom. While in general for the out-of-plane transfer higher activation energies are needed, the activation energy for migration of Al in-plane movement possesses with 1.56 ± 0.31 eV/atom the lowest activation energy for migration range overall in comparison to 4.02 ± 0.41 eV/atom for the Ti in-plane movement, which is slightly below the Al out-of-plane migration energy of 4.51 ± 0.19 eV/atom.

Under the assumption, that the atomic vacancy concentration is zero, the activation energy for diffusion via vacancies (Q_D) can be estimated by $Q_D = E_b + E_f$ [46]. This results in an activation energy for diffusion envelope of 2.19 ± 0.53 eV/atom for Al and 7.38 ± 0.69 eV/atom for Ti, when considering in-plane migration and 5.13 ± 0.41 eV/atom for Al and 11.77 ± 0.43 eV/atom for Ti for out-of-plane migration.

Hence, for both, in-plane and out-of-plane migration scenarios Al diffusion is predicted to be initiated at significantly lower temperatures than Ti migration.

TEM images of the cross-sectional morphology and corresponding EDX maps of the as deposited as well as the oxidized $Ti_{0.12}Al_{0.21}B_{0.67}$ coatings are shown in Fig. 3. For the as deposited coating, in agreement

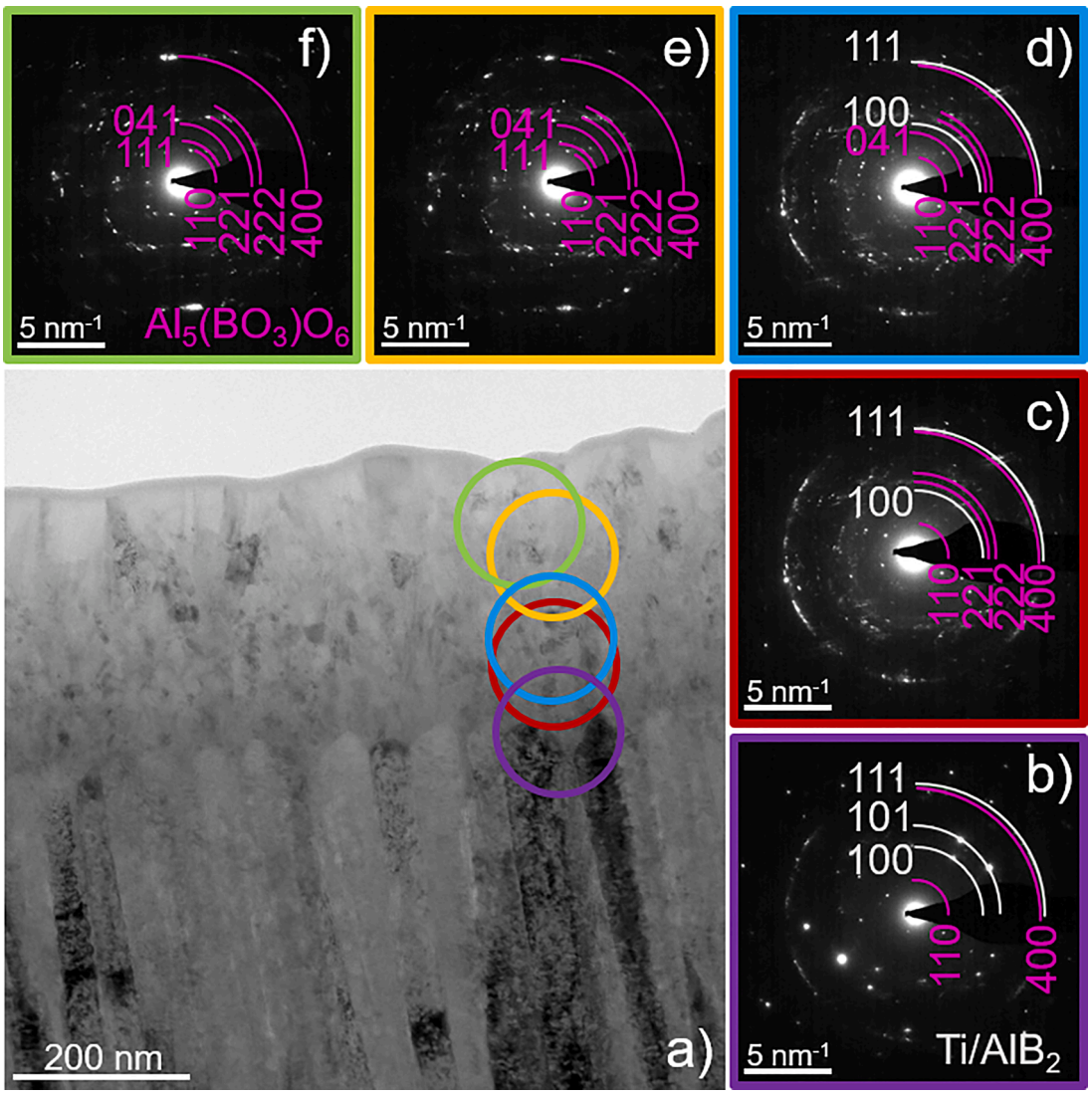


Fig. 5. TEM BF-image (a) and SAED patterns from different regions through the oxide layer (b-f) including the interface between scale and remaining film of a coating oxidized at 900 °C for 8 h. At the interface between coating and scale (b-c), the formation of amorphous regions as well as a continuous (nano-)crystalline layer is observed, while the grain size increases significantly towards the surface (d-f).

with Navidi et al. [27], a well-defined columnar morphology with a column width ranging from 10 to 65 nm is observed in Fig. 3(a). EDX and SAED (supplementary materials Figure S1) are consistent with the formation of a homogeneous solid solution between $Ti_{0.33}B_{0.67}$ and $Al_{0.33}B_{0.67}$. Additionally, a native oxide scale with a thickness of around 4 nm, containing mainly Al and O, is identified by STEM and EDX. Furthermore, it can be seen, that the column boundaries are enriched in Al and O, see Fig. 3(a). Hereby, an O gradient from the coating surface to the substrate interface can be observed, which appears to be caused by a change in grain boundary morphology: At the coating surface, the column boundaries are less dense than in the vicinity of the interface to the substrate. The cross sections of coatings annealed at 700 °C for 1, 4 and 8 h are shown in Fig. 3(b) to (d), respectively. Comparison between Fig. 3 (b) and Fig. 3(a) shows that, after oxidation for 1 h at 700 °C, the column asperity geometry changes from spherical-like towards facetted. HRSTEM analysis, shown in Figure S2, reveals the formation of $(1\bar{1}01)$ facets. While this topographic change appears to remain unaltered for longer holding times, see Fig. 3(c) and (d), the oxide scale thickness increases after oxidation for 1 and 4 h from the native oxide scale with a thickness of ~ 4 nm to 30 ± 8 nm and 41 ± 9 nm, respectively. After oxidation for 8 h at 700 °C, no significant changes in oxide scale thickness (42 ± 12 nm) or morphology could be observed.

STEM and EDX data shown in Fig. 4(a), indicate that the oxide layer formed after oxidation at 700 °C for 8 h consists primarily of Al and O (40 ± 2 at.% Al and 54 ± 2 at.% O) with a B content of 6 ± 2 at.%. The measured concentration of Ti is with ~ 0.3 at.% within the detection limit and hence a significant presence of Ti in the scale cannot be inferred. Raising the oxidation temperature to 800 and 900 °C, the oxide layer thickness measured after 8 h increases to 86 ± 12 nm and 333 ± 11 nm, respectively. As can be seen in Fig. 4(b), the scale is primarily composed of Al and O (34 ± 4 at.% Al and 61 ± 4 at.% O) containing 5 ± 2 at.% B, and is hence similar to the composition measured after oxidation at 700 °C. The formation of the Al-rich oxide layer is consistent with DFT data, see Fig. 2, as Al diffusion is predicted to be enabled at lower temperatures than Ti-diffusion. This prediction is based on envelope calculations taking the energy required to form vacancies on the metal sublattice as well as the associated migration barriers into account. While the morphology of the oxide scale surface after oxidation at 700 °C is smooth without apparent roughness see Fig. 4(c), after oxidation at 900 °C, see Fig. 4(d), the oxide scale shows evidence for pronounced faceting, see also Fig. 5(a).

To probe the structure evolution along the oxide layer thickness after oxidation at 900 °C for 8 h, SAED data was obtained from regions depicted in Fig. 5(a) ranging from the interface of the oxide scale with

Table 1
Phase analysis of SAED pattern shown in Fig. 5(f). The measured atomic distances in Å are identified to correlate with the formation of $Al_5(BO_3)O_6$ [48] in comparison to θ- [50] and κ- [51] alumina. The accuracy between the literature and measured value is given by a color scheme (green < 1 %, yellow < 2 %, orange ≥ 2 %, red = no fit).

	$Al_5(BO_3)O_6$			θ-Al_2O_3			κ-Al_2O_3		
d_m [Å]	(hkl)	d [48]	Δd/d [%]	(hkl)	d [50]	Δd/d [%]	(hkl)	d [51]	Δd/d [%]
5.35	(021)	5.37	0.4	(001)	5.46	2.0			
5.3	(110)	5.3	0.0						
4.36	(111)	4.37	0.2	(20-1)	4.54	4.0	(002)	4.48	2.7
3.7	(130)	3.75	1.3	(201)	3.56	3.9	(111)	3.79	2.4
3.37	(041)	3.37	0.0						
2.82	(200)	2.83	0.4	(400) (40-1)	2.88 2.84	2.1 0.7	(013)	2.81	0.4
2.66	(042) (220)	2.69 2.65	1.1 0.4	(002)	2.73	2.6	(031)	2.65	0.4
2.5	(221)	2.51	0.4	(111)	2.45	2.0	(122)	2.58	3.1
2.23	(240)	2.26	1.3	(401)	2.33	4.3	(211)	2.25	0.9
2.18	(222)	2.18	0.0	(31-1)	2.25	3.1	(123)	2.17	0.5
1.41	(400)	1.42	0.7	(20-4)	1.41	0.0	(205) (135)	1.44 1.44	2.1 2.1

the coating (Fig. 5(b)) to the oxide scale surface (Fig. 5(f)).

In the vicinity of the interface, the formation of a continuous (nano-) crystalline layer is witnessed by the fully developed diffraction rings shown in Fig. 5(c). Additionally, the presence of amorphous regions is indicated by broad and diffuse diffraction rings, see Fig. 5(c). Grain size and crystallinity within the scale increase with increasing distance to the coating/scale interface, see Fig. 5(c) to (f), where the formation of crystallites with grain sizes < 70 nm is evident from Fig. 5(a). With increasing distance from the coating/oxide interface, the intensity of reflexes corresponding to the diborides decreases, while the intensity corresponding to the oxide scale increases [47–49].

Phase analysis, based on the SAED data presented in Table 1, reveals the formation of $Al_5(BO_3)O_6$ crystallites [48], while the presence of initially expected alumina polymorphs appears to be unlikely. All major diffraction signals can be exclusively explained by the presence of $Al_5(BO_3)O_6$ in the oxide scale, whereby the (110) and (041) peaks are unique to orthorhombic $Al_5(BO_3)O_6$ and cannot be explained by the presence of alumina polymorphs. Additionally, the measured interplanar spacings are in very good agreement with the ICSD (PDF 01–072–1931) [48] data with a deviation of 0.5 ± 0.5 %, compare Table 1 and Figure S3. In contrast, the best fit for alumina, especially for lower atomic distances, is for θ- and κ-alumina, see Figure S3, whereby the deviation to the ICSD (PDF 01–079–1559 and 01–088–0107) [50, 51] data of 2.5 ± 1.3 % for θ-alumina and 1.6 ± 1 % for κ-alumina are significantly larger than for $Al_5(BO_3)O_6$. Thereby, taking the unique peaks as well as the deviations to the ICSD data into account, the presence of $Al_5(BO_3)O_6$ is clearly established. However, the here obtained diffraction data also shows very good agreement with orthorhombic $Al_{18}B_4O_{33}$ (PDF 00–032–0003). Both, the chemical and structural differences between the two borate phases are minute. While the O concentration in both phases is with 60 at.% constant, the differences in B and Al concentrations are 0.6 at.% and hence not resolvable with the composition probes employed here. The maximum relative deviation of experimentally observed diffraction signals, within the interplanar spacing range of $1.4 \leq d \leq 6.0$ Å between $Al_{18}B_4O_{33}$ (PDF 00–032–0003) and $Al_5(BO_3)O_6$ (PDF 01–072–1931), is 0.1 %. Hence, the two aluminoborates, $Al_{18}B_4O_{33}$ and $Al_5(BO_3)O_6$, cannot be differentiated with the acquired data, as the composition and structural deviations cannot be resolved.

To critically appraise the preferential Al diffusion notion, predicted by DFT envelope calculations, the spatially and temporally resolved chemical composition in regions adjacent to the coating/scale interface was measured via EDX line scans after oxidation for 1, 4 and 8 h at 700 °C and compared to the as deposited state, see Fig. 6(a) to (d) and Figure S4.

For all investigated coatings, the O concentration is significantly higher compared to the data measured by ERDA [27]. This is likely due to oxidation of the lamellae sides as a consequence of atmosphere exposure during transfer after lift-out prior to TEM imaging. Therefore, only O concentration variations within one sample are discussed further, while the Al/metal ratio is compared between the coatings.

The O content of the as deposited coating depicted in Fig. 6(a) is steadily increasing over the 100 nm thick region adjacent to the surface, where the interfacial region between the 4 nm thick native oxide scale (not distinguishable) and the coating is marked in red, see Fig. 3(a) and Figure S4 (a). The increase of oxygen concentration in the region below the 4 nm thick native oxide and the coating/scale interface, marked in red, can be attributed to preferential O incorporation at grain boundaries and triple junctions due to atmosphere exposure. In contrast to the O content, a decrease in the Al/metal ratio in a region of 20 nm below the native oxide, can be observed. It is evident that Al forming the native oxide scale has diffused out of this region.

Upon oxidation at 700 and 800 °C, see Fig. 6(b) to (e), the formation of the oxide scale, marked in green, is evident while the Al/metal ratio within the coating in the region adjacent to the interfacial region, marked in red, is within the range of 0.65 ± 0.05. Furthermore, a drastic increase in the Al/metal ratio can be seen in the interfacial region, marked in red, for all at 700 and 800 °C oxidized samples. This is in stark contrast to the chemical composition measured in the interfacial region of the as deposited sample, shown in Fig. 6(a), where Al depletion by the

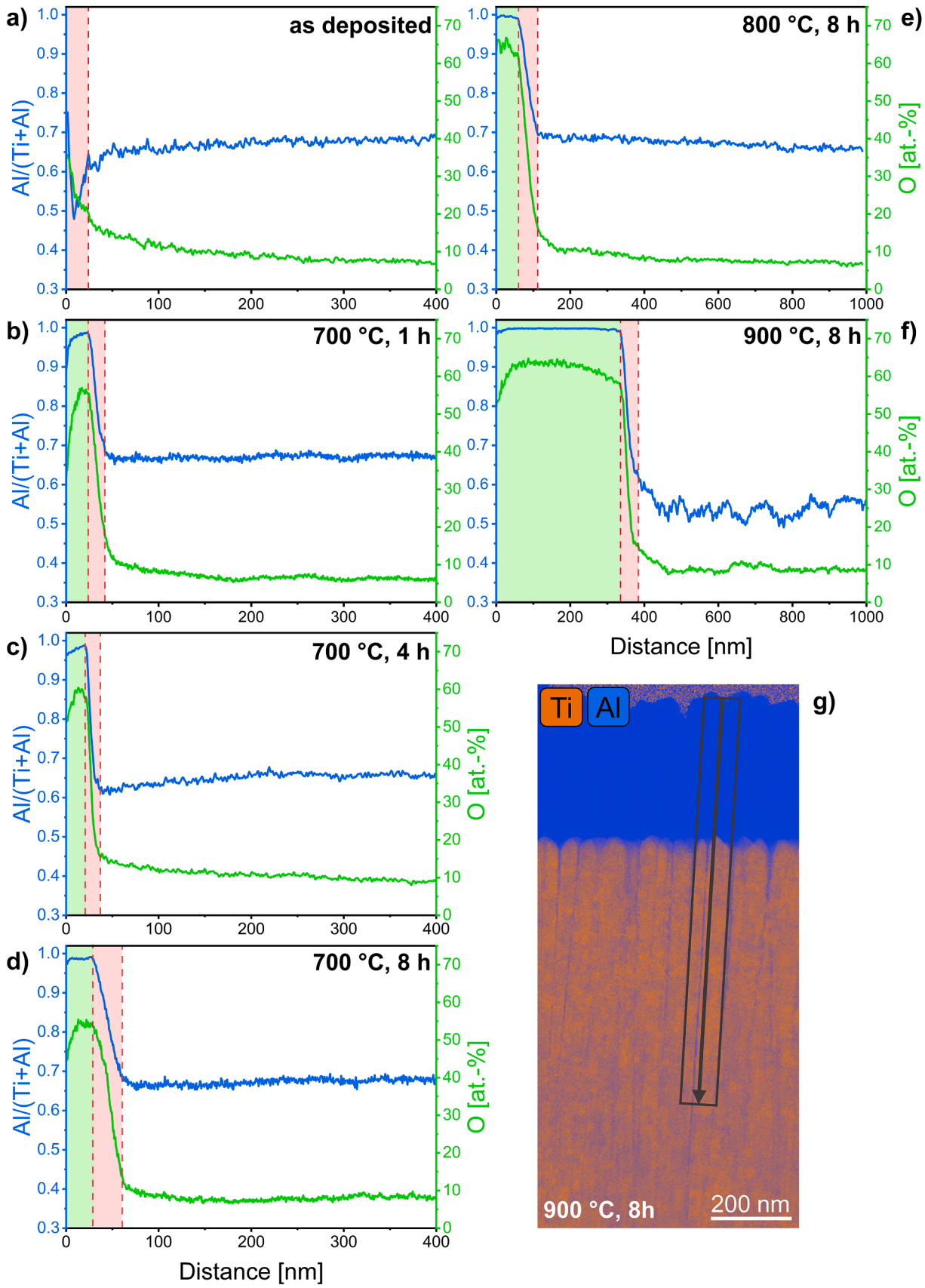


Fig. 6. Linescans of as deposited (a) and oxidized $Ti_{0.12}Al_{0.21}B_{0.67}$ coatings at 700 °C for 1 h (b), 4 h (c) and 8 h (d). Diffusion of Al over the length of the coating can be seen. When increasing the oxidation temperature to 800 °C (e) and 900 °C (f), a decrease in the Al/metal ratio is shown with segregation of TiB_2 and AlB_2 visible in (g). The regions marked in green and red in images (a) to (f) correspond to the oxide scale and the interfacial regions between the scale and the unoxidized coating.

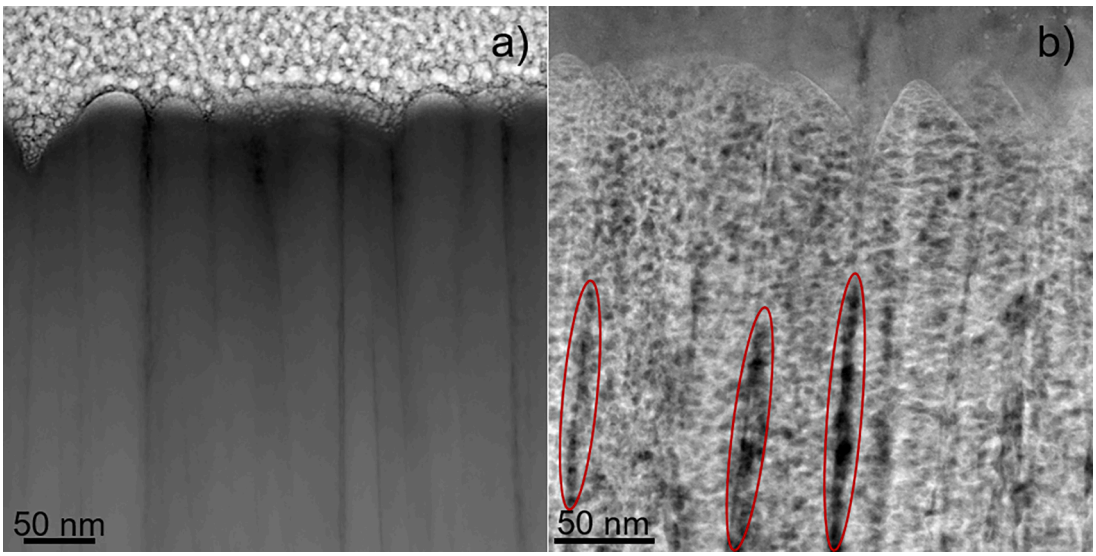


Fig. 7. STEM HAADF images of an as deposited coating (a) and oxidized at 900 °C for 8 h (b).

native oxide scale formation causes a decrease in the Al/metal ratio from 0.65 to 0.48 in the region marked in red. Hence, it is evident that the Al depleted region, only identified for the as deposited coating, could not be replenished by Al diffusion from the reservoir in the as deposited coating. Contrarily at $\geq$ 700 °C, this kinetic limitation is overcome as witnessed by the disappearance of the Al depleted region beneath the interfacial region, marked in red in Fig. 6(b) to (e) as a consequence of the Al redistribution from the Al reservoir of the coating resulting in a homogeneous distribution of Al over the coating thickness.

Further evidence for thermally activated Al diffusion, enabling the formation of the oxide scale, is shown by HR-EDX in Figure S5 in the form of an Al pile up at the coating/scale interface after oxidation at 700 °C for 8 h. Fig. 6(f) depicts the EDX linescans after oxidation at 900 °C for 8 h. While the composition variations measured in the interfacial region, marked in red, correspond to observations made at lower oxidation temperatures, the oxide scale thickness increased to 333 ± 11 nm and the Al/metal ratio within the coating ranges from 0.49 to 0.58.

Assuming that the oxide layer consists exclusively of $Al_5(BO_3)O_6$ with a density of 2.94 g cm^{-3} [48] and that all Al atoms forming the scale are supplied from the reservoir of the unoxidized coating, the corresponding Al concentration decrease can be calculated: After oxidation for 8 h at 800 and 900 °C, the oxide scale thicknesses of 86 ± 12 nm and 333 ± 11 result in a decrease of the corresponding Al concentrations by 1.7 ± 0.2 at.% and 6.7 ± 0.2 at.% respectively. Therefore, a significant decrease in the Al content over the whole unoxidized coating thickness, indicative of the diffusion mediated redistribution of Al from the unoxidized coating to the oxide scale, can be observed after oxidation at 900 °C. However, after oxidation at 800 °C, the measured Al concentration variation is within the EDX detection limit, consequently the comparatively low Al requirement for oxide scales at temperatures < 900 °C could not be resolved.

Hence, it is evident that scale growth is mediated by Al diffusion from the unoxidized coating to the oxide scale, while no evidence for diffusion of Ti could be obtained at oxidation temperatures < 900 °C, see Fig. 6(b) to (e). The fact that Al diffusion enables scale formation, while Ti diffusion is inactive, see Fig. 6(b) to (e), is consistent with the lower energies necessary for Al mass transport compared to Ti as calculated by DFT (Fig. 2). Furthermore, as the oxidation temperature is increased to 900 °C, diffusion of both Al and Ti is enabled, leading to the formation of Al- and Ti-rich regions, represented by modulations in the line scan shown in Fig. 6(f) as well as by the differently colored regions in Fig. 6 (g). Again, these composition variations, caused by diffusion as discussed above, are in very good agreement with the DFT calculations presented in Fig. 2.

Completing the chemical information given above, the *Z* contrast in the STEM images in Fig. 7 shows that the formation of Al- and Ti-rich regions within the columns is mediated by diffusion of Al as well as Ti. This observation is consistent with thermal stability investigations, where the formation of Al- and Ti-rich regions was shown to be caused by decomposition of the metastable solid solution of TiB_2 and AlB_2 [52] via spinodal decomposition. In contrast to the as deposited coating, shown in Fig. 7(a), the decomposition of the $(Ti,Al)B_2$ solid solution after oxidation is characterized by the brighter (Ti-rich) and darker (Al-rich) regions, see Fig. 7(b). As a consequence of Al diffusion and Al incorporation in the oxide scale, the formation of elongated porous regions (marked in red) with sizes > 100 nm in length and a few nm in width is observed.

Atom probe tomography was performed after oxidation for 8 h at 700 °C and at 900 °C and the specimens were extracted from in-plane direction at a depth of ~300 nm below the oxide/coating interface. Consistent with the EDX maps shown in Fig. 3 and the associated discussion, it is evident from the spatially resolved analysis of the O content depicted in Fig. 8(a) and (b) that multiple column boundaries were probed in the sample oxidized at 700 °C. Locally, the Al and O content at the column boundaries increases from 26 ± 2 to 39 ± 2 at.% and from 2 ± 1 to 9 ± 1 at.% (distance of ~60 nm). After oxidation at 900 °C, the APT data show elemental distributions in Fig. 8(c) and (d), consistent with the above presented Al redistribution notion. In contrast to the coating oxidized at 700 °C (see Fig. 8(a) and (b)) as well as the as-deposited sample (see supplementary Figure S6), the formation of Al- and Ti-rich regions, is witnessed by the variation of the Al/(Ti+Al) ratio between 0.31 ± 0.05 and 0.59 ± 0.10 (distance of 16 to 18 nm, Fig. 8 (e)), indicating spinodal decomposition. From the same data set, the grain boundary composition ranges can be extracted. The grain boundaries contain up to 51 ± 2 at.% Al and 36 ± 2 at.% O, while the Ti and B content are reduced to 7 ± 1 at.% and 6 ± 1 at.%, respectively (distance of 27 to 28 nm).

The results observed here show both, similarities and differences to recently published thermal stability data for $Ti_{0.12}Al_{0.21}B_{0.67}$ coatings where after 1 h at 1000 °C spinodal decomposition was witnessed based on EDX and APT data [52]. Spinodal decomposition within the grains occurs upon annealing [52] as well as upon oxidation. In contrast to the coatings annealed at 1000 °C for 1 hour [52], no indication of AlB_{12} formation could be obtained after oxidation at 900 °C for 8 h, indicating that the oxidation behavior at these conditions is not limited by thermal decomposition.

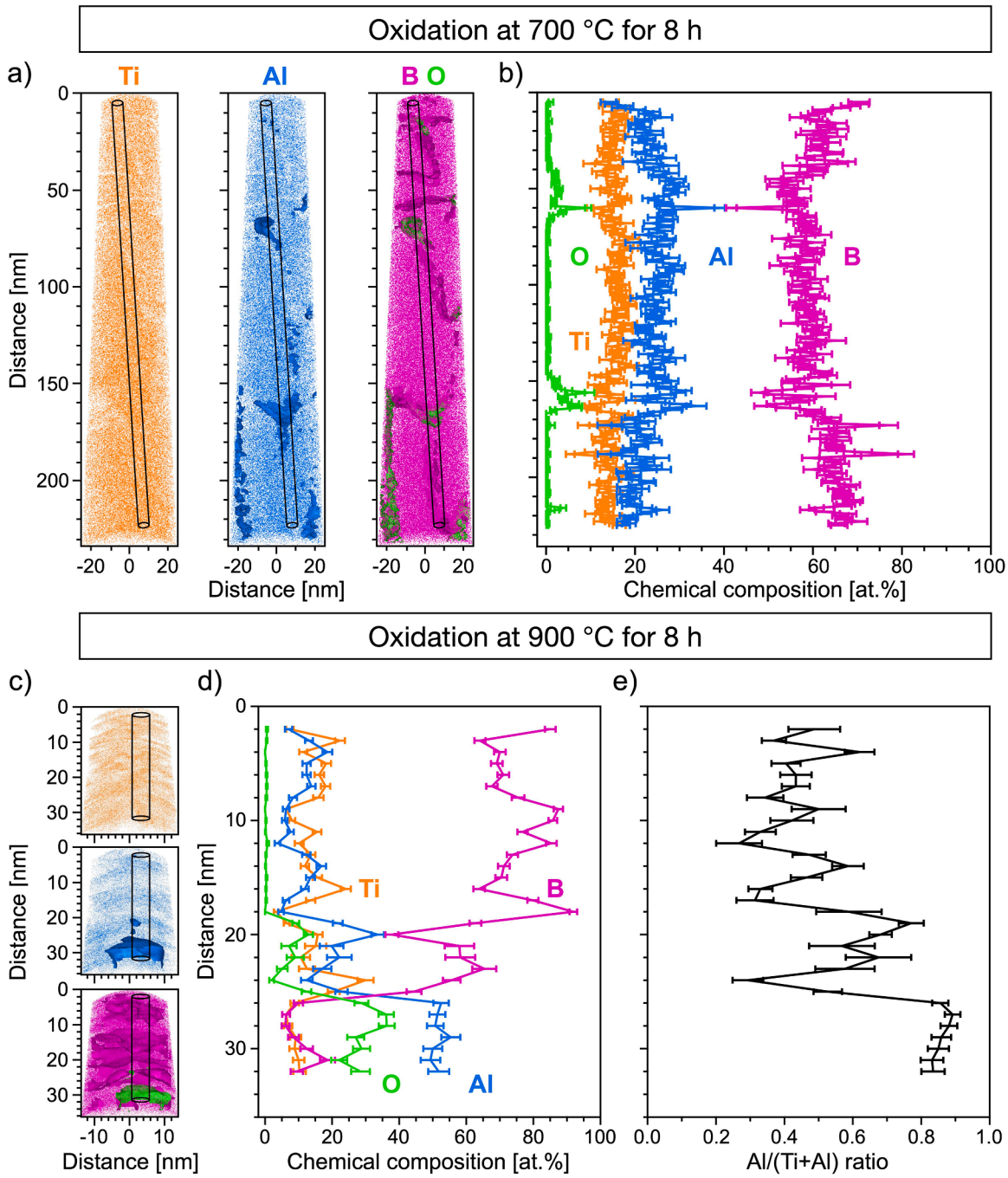


Fig. 8. Atomic positions, isoconcentration surfaces (Al ≥ 30 at.%, *B* ≥ 70 at.%, *O* ≥ 4 at.%) and composition profile obtained by atom probe tomography of an in-plane specimen taken from a depth of ~300 nm below the surface for the sample oxidized at 700 °C for 8 h (a) and (b) and 900 °C for 8 h (c) and (d) as well as the Al/(Ti+Al) ratio for the 900 °C sample (e). The cylinders exhibit a diameter of 5 nm.

4.1. Proposed oxidation mechanism

The here unraveled oxidation mechanism for passivating [27], stoichiometric $Ti_{0.12}Al_{0.21}B_{0.67}$ is summarized in Fig. 9. A columnar structure is observed in the as deposited state, exhibiting grain boundaries that are enriched in Al and O compared to the grains. Atmosphere exposure of the as deposited coating results in the formation of a 4 nm thick native oxide layer, formed by Al diffusion from a 20 nm thick region adjacent to the scale coating interface as witnessed by EDX. Upon oxidation, the topography changes from spherically terminated columns to more faceted terminated columns.

Upon oxidation, a scale layer forms, which is amorphous at 700 °C and transforms to (nano-)crystalline at 900 °C, consisting of 34 ± 4 at.% of Al, 61 ± 4 at.% of O and 5 ± 2 at.% of B at 900 °C. The scale layer is formed by Al diffusion from the unoxidized coating to the oxide scale, which requires, according to DFT predictions compiled in Fig. 2, a significantly lower energy for mass transport on the metal sublattice than Ti. Hence, based on these DFT predictions, the previously unexplained superior oxidation behavior compared to $Ti_{0.27}Al_{0.21}N_{0.52}$ coatings can be understood via the here reported formation of a passivating boron containing oxide scale, while for $Ti_{0.27}Al_{0.21}N_{0.52}$ coatings, the formation of a Ti and Al containing oxide scale is observed [33].

Diffusion through the passivating oxide scale is limiting the

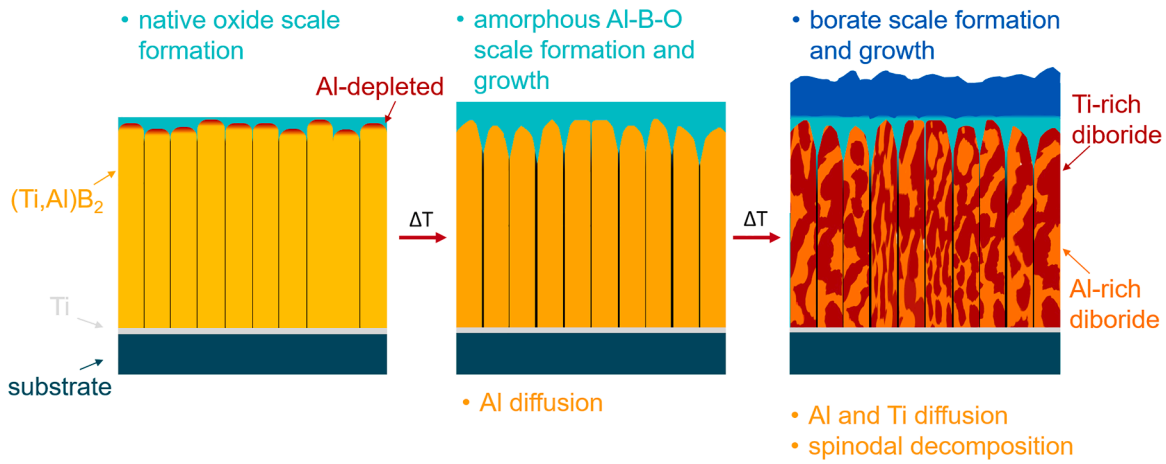


Fig. 9. Schematic representation of the here identified oxidation mechanism for $Ti_{0.12}Al_{0.21}B_{0.67}$.

oxidation kinetics. The homogeneous Al profile throughout the unoxidized coatings, see Fig. 6, is enabled by Al diffusion, within the grains as well as along grain boundaries, in the unoxidized coating as Al required for scale formation is upon oxidation replenished for all oxidation conditions studied here, except for 900 °C and 8 h. At this condition, the amount of Al required to form the scale can no longer be replenished by Al redistribution from the unoxidized coating as witnessed by an overall decrease of the inhomogeneous Al distribution measured by EDX, see Fig. 6(f). Simultaneously, spinodal decomposition of the $(Ti,Al)B_2$ solid solution into Al-rich and Ti-rich regions within the grains can be observed with EDX, see Fig. 6(f) and (g), HRSTEM, see Fig. 7 and APT, see Fig. 8(c) to (e), which is enabled by the onset of Ti diffusion predicted to occur at higher temperatures compared to Al, see Fig. 2. Hence, at 900 °C simultaneous diffusion of Al and Ti enables spinodal decomposition. The fact that this observation is in contrast to the formation of Ti-rich crystallites by nucleation and growth as reported by Mockuté et al. [32] for B-rich tissue phase containing $Ti_{0.17}Al_{0.07}B_{0.76}$ $[(Ti_{0.71}Al_{0.29})B_{3.08}]$ annealed at 1000 °C for 1 h, underlines the significance of the chemical composition, specifically deviations from stoichiometry, for the oxidation behavior of $(Ti,Al)B_2$ based coatings.

The exceptional oxidation behavior of $Ti_{0.12}Al_{0.21}B_{0.67}$ can be explained by the formation of the B containing, amorphous and (nano-) crystalline aluminoborate layer, caused by the diffusion of Al from the unoxidized coating to the scale.

Comparing the oxidation behavior at 900 °C after 2 h of a 1.3 μm thick $Ti_{0.27}Al_{0.21}N_{0.52}$ coating with the here considered $Ti_{0.12}Al_{0.21}B_{0.67}$ coating, where both coatings exhibit, within the measurement error an identical Al concentration, it is evident that the nitride coating is fully oxidized [33], while the scale thickness measured on $Ti_{0.21}Al_{0.21}B_{0.67}$ is 333 ± 11 nm at the same temperature but at a 4 times longer oxidation time. At these conditions, the superior oxidation behavior of the diboride compared to the nitride coating, both with an Al concentration of 21 at.%, is hence due to the passivating capacity of the borate scale formed on the boride as compared to the mixed, Ti and Al containing oxide scale forming on the nitride [33].

5. Conclusion

The high temperature oxidation behavior of $Ti_{0.12}Al_{0.21}B_{0.67}$ coatings was investigated in an electron microscopy study, supported by ab initio calculations. STEM imaging revealed the formation of a native 4 nm thick Al-rich oxide scale as well as the incorporation of O at the grain boundaries in the as deposited state. Upon oxidation, thicker scales consisting primarily of Al and O with a small B content were formed, which appear to be amorphous at 700 °C and (nano-)crystalline at 900 °C. The average activation energies of migration and the formation energy of vacancies, which were obtained by DFT calculations, proved to be lower for Al than for Ti, suggesting that Al diffusion is initiated at lower temperatures than Ti diffusion. These predictions are consistent with TEM, EDX and APT data.

Upon oxidation at 700 and 800 °C, the formation and growth of an oxide scale composed of Al and O as well as ~5 at.% B is mediated by Al diffusion within the unoxidized $Ti_{0.12}Al_{0.21}B_{0.67}$ phase, replenishing the Al required for scale formation.

After oxidation at 900 °C for 8 h, a crystalline aluminoborate layer was identified by EDX and SAED analysis. Additionally, spinodal decomposition of the $Ti_{0.12}Al_{0.21}B_{0.67}$ phase into Al- and Ti-rich boride regions is witnessed. The spinodal decomposition is enabled by concurrent diffusion of Al and Ti, setting in only at higher temperatures and longer holding times due to the higher averaged energies required for Ti migration as compared to Al, consistent with DFT predictions. Overall, the extraordinary oxidation resistance of $Ti_{0.12}Al_{0.21}B_{0.67}$ is enabled by energetically preferred Al diffusion leading to the formation of a passivating, amorphous oxide scale, predominantly comprised of Al, O and B. At higher temperatures, the transformation of the amorphous oxide scale to (nano-)crystalline $Al_5(BO_3)O_6$ occurs, while simultaneously, the onset of Ti diffusion in combination with the Al diffusion enables spinodal decomposition of the $Ti_{0.12}Al_{0.21}B_{0.67}$ phase into Ti- and Al-rich regions. In comparison to $Ti_{0.27}Al_{0.21}N_{0.52}$ coatings, with an identical Al concentration, the superior oxidation resistance of stoichiometric $Ti_{0.12}Al_{0.21}B_{0.67}$ coatings at 900 °C can be rationalized based on the formation of a passivating (nano-)crystalline aluminoborate scale layer, rendering the here investigated boride with a 333 ± 11 nm thick scale layer after oxidation for 8 h, while the $Ti_{0.27}Al_{0.21}N_{0.52}$ coating is oxidized completely after 2 h [33].

CRediT authorship contribution statement

Sebastian Lellig: Writing – original draft, Visualization, Validation, Software, Investigation, Formal analysis, Data curation, Conceptualization. **Amir Hossein Navidi Kashani:** Writing – review & editing, Investigation, Formal analysis, Data curation. **Peter Schweizer:** Writing – review & editing, Visualization, Software, Investigation, Formal analysis, Data curation. **Marcus Hans:** Writing – review & editing, Writing – original draft, Visualization, Software, Investigation, Formal analysis, Data curation. **Ganesh K. Nayak:** Writing – review & editing, Writing – original draft, Visualization, Software, Formal analysis, Data curation. **Johann Michler:** Writing – review & editing, Supervision, Resources, Funding acquisition, Conceptualization. **Jochen M. Schneider:** Writing – original draft, Supervision, Resources, Project administration, Funding acquisition, Conceptualization.

Declaration of competing interest

The authors declare that they have no known competing financial interests or personal relationships that could have appeared to influence the work reported in this paper.

Acknowledgments

The research was funded by the German Research Foundation (DFG SCHN 735/47–1). The authors would like to acknowledge the Jülich-Aachen Research Alliance (JARA) HPC section at the IT Center of RWTH Aachen University for the supplied computing time as part of the projects JARA0151.

Supplementary materials

Supplementary material associated with this article can be found, in the online version, at doi:10.1016/j.actamat.2024.120662.

References

[1] R.G. Munro, Material properties of titanium diboride, J. Res. Natl. Inst. Stand. Technol. 105 (5) (2000) 709.
[2] M. Berger, S. Hogmark, Evaluation of TiB2 coatings in sliding contact against aluminium, Surf. Coat. Technol. 149 (1) (2002) 14–20.
[3] A. Dranenko, V. Lavrenko, V. Talash, Corrosion resistance of nanostructured TiB2 films in 3% NACl solution, Powder Metall. Metal Ceram. 49 (3) (2010) 174–178.
[4] B. Zou, et al., Mechanical properties and microstructure of TiB2–TiC composite ceramic cutting tool material, Int. J. Refractory Metals Hard Mater. 35 (2012) 1–9.
[5] F.S. Moghanlou, et al., A numerical approach to the heat transfer in monolithic and SiC reinforced HfB2, ZrB2 and TiB2 ceramic cutting tools, Ceram. Int. 45 (13) (2019) 15892–15897.
[6] S. Grigoriev, et al., The study of radius end mills with TiB2 coating when milling a nickel alloy, Materials 16 (6) (2023) 2535.
[7] M.C. Shaw, J. Cookson, Metal Cutting Principles, Oxford university press, New York, 2005. Vol. 2.
[8] X. Huang, et al., Hypervelocity impact of TiB2-based composites as front bumpers for space shield applications, Mater. Des. 97 (2016) 473–482.
[9] N. Gupta, et al., Ballistic studies on TiB 2-Ti functionally graded armor ceramics, Def. Sci. J. 62 (6) (2012).
[10] W.G. Fahrenholtz, G.E. Hilmas, Ultra-high temperature ceramics: materials for extreme environments, Scr. Mater. 129 (2017) 94–99.
[11] P. Mayrhofer, et al., Self-organized nanocolumnar structure in superhard TiB 2 thin films, Appl. Phys. Lett. 86 (13) (2005) 131909.
[12] P.H. Mayrhofer, Thermal stability and self-arrangement of nanocrystalline hard coatings. Nanostructured Thin Films and Nanodispersion Strengthened Coatings, Springer, 2004.
[13] M. Berger, M. Larsson, S. Hogmark, Evaluation of magnetron-sputtered TiB2 intended for tribological applications, Surf. Coat. Technol. 124 (2–3) (2000) 253–261.
[14] M.N. Polyakov, et al., Microstructure-driven strengthening of TiB2 coatings deposited by pulsed magnetron sputtering, Surf. Coat. Technol. 368 (2019) 88–96.
[15] S.K. Padamata, et al., Wettable TiB2 cathode for aluminum electrolysis: a review, J. Sustain. Metall. 8 (2) (2022) 613–624.
[16] J. Li, et al., Research progress in TiB 2 wettable cathode for aluminum reduction, Jom 60 (2008) 32–37.
[17] A.V. Cooke, W.M. Buchta, Use of TiB2 cathode material: demonstrated energy conservation in VSS cells. Essential Readings in Light Metals: Volume 4 Electrode Technology for Aluminum Production, Springer, 1985, pp. 1153–1163.
[18] L. Xi, et al., High-temperature wetting and interfacial interaction between liquid Al and TiB 2 ceramic, J. Mater. Sci. 50 (2015) 2682–2690.
[19] R. He, et al., Anti-corrosion and conductivity of titanium diboride coating on metallic bipolar plates, Corros. Sci. 170 (2020) 108646.
[20] C. Monticelli, et al., The corrosion behaviour of titanium diboride in neutral chloride solution, Corros. Sci. 43 (5) (2001) 979–992.
[21] Y. Diao, K. Zhang, Microstructure and corrosion resistance of TC2 Ti alloy by laser cladding with Ti/TiC/TiB2 powders, Appl. Surf. Sci. 352 (2015) 163–168.
[22] X. Cai, et al., Unmasking the anomalous rapid oxidation of refractory TiB2 at low temperatures, J. Eur. Ceram. Soc. 41 (10) (2021) 5100–5108.
[23] C. Fuger, et al., Revisiting the origins of super-hardness in TiB2+z thin films – Impact of growth conditions and anisotropy, Surf. Coat. Technol. 446 (2022) 128806.
[24] A. Tampieri, A. Bellosi, Oxidation of monolithic TiB2 and of Al2O3-TiB2 composite, J. Mater. Sci. 28 (3) (1993) 649–653.
[25] B. Bakhit, et al., Improving the high-temperature oxidation resistance of TiB2 thin films by alloying with Al, Acta Mater. 196 (2020) 677–689.
[26] V. Voitovich, V. Lavrenko, V. Adejev, High-temperature oxidation of titanium diboride of different purity, Oxidat. Metals 42 (1) (1994) 145–161.
[27] A.H. Navidi Kashani, et al., Synthesis and Oxidation Behavior of Ti0. 35Al0. 65By (y= 1.7–2.4) Coatings, Surf. Coat. Technol., 2022 128190.
[28] J. Thörnberg, et al., Oxidation resistance and mechanical properties of sputter-deposited Ti0. 9Al0. 1B2-y thin films, Surf. Coat. Technol. (2022) 128187.
[29] S. Mollica, et al., Effect of aluminium ion implantation on the oxidation resistance of DC magnetron sputter-deposited TiB2 thin films, Surf. Coat. Technol. 177 (2004) 185–197.
[30] M. Stüber, et al., Microstructure of Al-containing magnetron sputtered TiB2 thin films, Thin Solid Films 688 (2019) 137361.
[31] N. Nedfors, et al., Influence of the Al concentration in Ti-Al-B coatings on microstructure and mechanical properties using combinatorial sputtering from a segmented TiB2/AlB2 target, Surf. Coat. Technol. 364 (2019) 89–98.
[32] A. Mockuté, et al., Age hardening in (Ti1-xAlx) B2+ Delta thin films, Scr. Mater. 127 (2017) 122–126.
[33] A.H. Navidi Kashani, et al., Morphology, mechanical properties, and oxidation behavior of stoichiometric Ti0.33-xAlxB0.67 coatings (x = 0.04, 0.15, 0.21, and 0.28), Acta Mater. 270 (2024) 119829.
[34] M. Hans, et al., Probing the onset of wurtzite phase formation in (V, Al) N thin films by transmission electron microscopy and atom probe tomography, Surf. Coat. Technol. (2022) 128235.
[35] G.K. Nayak, et al., On correlations between local chemistry, distortions and kinetics in high entropy nitrides: an ab initio study, Acta Mater. (2023) 118951.
[36] K. Thompson, et al., Three-dimensional atom mapping of dopants in Si nanostructures, Appl. Phys. Lett. 87 (5) (2005) 052108.
[37] S.-H. Wei, et al., Electronic properties of random alloys: special quasirandom structures, Phys. Rev. B 42 (15) (1990) 9622.
[38] G. Kresse, J. Furthmüller, Efficiency of ab-initio total energy calculations for metals and semiconductors using a plane-wave basis set, Comput. Mater. Sci. 6 (1) (1996) 15–50.
[39] G. Kresse, J. Furthmüller, Efficient iterative schemes for ab initio total-energy calculations using a plane-wave basis set, Phys. Rev. B 54 (16) (1996) 11169.
[40] J.P. Perdew, et al., Restoring the density-gradient expansion for exchange in solids and surfaces, Phys. Rev. Lett. 100 (13) (2008) 136406.
[41] P.E. Blöchl, Projector augmented-wave method, Phys. Rev. B 50 (24) (1994) 17953.
[42] H.J. Monkhorst, J.D. Pack, Special points for Brillouin-zone integrations, Phys. Rev. B 13 (12) (1976) 5188.
[43] M. Methfessel, A. Paxton, High-precision sampling for Brillouin-zone integration in metals, Phys. Rev. B 40 (6) (1989) 3616.
[44] D. Sheppard, R. Terrell, G. Henkelman, Optimization methods for finding minimum energy paths, J. Chem. Phys. 128 (13) (2008) 134106.
[45] G.K. Nayak, M.N. Popov, D. Holec, Pressure- and temperature-dependent diffusion from first-principles: a case study of V and Ti in a TiN matrix, Surf. Coat. Technol. 422 (2021) 127491.
[46] G. Gottstein, Physical Foundations of Materials Science, Springer, 2004. Vol. 3.
[47] J.T. Norton, H. Blumenthal, S. Sindeband, Structure of diborides of titanium, zirconium, columbium, tantalum and vanadium, JOM 1 (10) (1949) 749–751.
[48] E.V. Sokolova, et al., Crystal Structure of Synthetic ortho-3-borate, Al_5(BO_3)O_6. in Doklady Akademii Nauk, Russian Academy of Sciences, 1978.
[49] E.J. Felten, The preparation of aluminum diboride, AlB21, J. Am. Chem. Soc. 78 (23) (1956) 5977–5978.
[50] R.-S. Zhou, R.L. Snyder, Structures and transformation mechanisms of the η, γ and θ transition aluminas, Acta Crystallographica Sect. B 47 (5) (1991) 617–630.
[51] B. Ollivier, et al., Crystal structure of κ-alumina: an X-ray powder diffraction, TEM and NMR study, J. Mater. Chem. 7 (6) (1997) 1049–1056.
[52] A.H. Navidi Kashani, et al., Temporally-resolved decomposition of Ti0. 12Al0. 21B0. 67 thin films at 1000°C, Surf. Coat. Technol. (2024) 131026.